Modelling the phosphorus dynamics of VPO catalyst during *n*-butane oxidation: A *μ*-reactor study

Scott D. Anderson [a,*], Martin Kutscherauer [b], Gregor D. Wehinger [b], Gerhard Mestl [c], Thomas Turek [a]

[a] *Institute of Chemical and Electrochemical Process Engineering, Clausthal University of Technology, Leibnizstraße 17, Clausthal-Zellerfeld, 38678, Germany*
[b] *Institute of Chemical Process Engineering, Karlsruhe Institute of Technology, Fritz-Haber-Weg 2, Karlsruhe, 76131, Germany*
[c] *Clariant AG, Waldheimer Strasse 15, Heufeld, 83052, Germany*

ABSTRACT

Production of maleic anhydride from *n*-butane is carried out in large fixed-bed reactors, which face a multitude of challenges, amongst them the removal of heat produced by the reaction, alongside a transient increase in activity due to phosphorus loss from the catalyst, causing a shift in selectivities and loss in target product yield. Improved modelling can aid in a better understanding of the involved processes, such that operating policies can be optimized. However, this necessitates the coupling of models for all subprocesses, that are parameterised independently of one another. To date, especially the phosphorus dynamics are not well understood and lack models to describe them. Experiments involving μ-reactor phosphorus dosing under transport limitation-free conditions are reported, investigating the underlying mechanisms of the phosphorus dynamics. Based on this data, an activity model comprising only four parameters is developed. Results indicate that a site-blocking mechanism plays a role in the phosphorus dynamics.

1. Introduction

Maleic anhydride (MA, IUPAC: Furan-2,5-dione) is an organic molecule comprising several functional groups, which make it a suitable intermediate for subsequent chemical modification. It contains two carboxylic groups, a heterocyclic ring and a C=C double bond (Müller et al., 2022; Felthouse et al., 2001; Lohbeck et al., 2000). Due to its particular chemical properties, MA is used in the chemical industry, with the majority market being unsaturated polyester resins for construction (Guan et al., 2018; Volta, 2000). However, an increasing awareness for the need of sustainable materials has seen MA become relevant in the production of biodegradable plastics, too (Raquez et al., 2008b,a; Dammak et al., 2020). Other common products relying on MA include co-polymers, lubricant additives, and selected bulk chemicals (Guan et al., 2018; Volta, 2000).

To date, the most common synthesis route relies on the selective oxidation of *n*-butane over vanadium-phosphorus-oxide (VPO), a mixed-metal-oxide catalyst (Bartley et al., 2008; Trifirò and Grasselli, 2014). With a global production capacity of more than 5 Million t/a, it is the most widely applied selective oxidation reaction in the world (Denny, 2024). It is characterized by its distinctly exothermic nature ($\Delta_R H^0 = -1236\,\mathrm{kJ\,mol^{-1}}$ Felthouse et al., 2001; Lesser et al., 2016), which poses a

significant challenge for heat removal. Simultaneously, the inherently low reactivity of *n*-butane requires the reaction to be carried out at elevated temperatures (Müller et al., 2022). Despite the existence of specially developed reactor concepts (Lerou and Mills, 1993), large multitubular reactors ($3\,m < L < 6.5\,m$) remain the workhorse of MA production to date (Ballarini et al., 2006; Lohbeck et al., 2000; Müller et al., 2022). They usually consist of several ten-thousand slender reactor tubes ($20\,mm < d_T < 25\,mm$), providing good heat transfer properties through a high surface to volume ratio, cooled via a molten salt bath at operating temperatures in the range of 380 °C to 430 °C. The feed, delivered at head pressures around $1\,\mathrm{barg}$ to $2\,\mathrm{barg}$, consists of 1 vol% to 2 vol% *n*-butane in compressed ambient air (Volta, 2000; Lesser et al., 2016; Müller et al., 2022).

Despite this dilute feed mixture, distinct hot-spots of $50\,K$ to $70\,K$ above cooling temperature can occur as a result of insufficient heat removal (Lesser et al., 2016; Müller et al., 2022). Higher temperatures and the accompanying higher conversion levels generally shift the selectivity away from MA and towards CO_x (CO and CO_2) and increase the catalytic activity - it is well documented that consecutive oxidation of MA is favoured when *n*-butane conversion exceeds 70 % (Trifirò and Grasselli, 2014; Ballarini et al., 2006; Wellauer et al., 1986). In addition to this innate issue of the reaction itself, high temperatures can

---

* Corresponding author.
E-mail addresses: anderson@icvt.tu-clausthal.de (S.D. Anderson), martin.kutscherauer@kit.edu (M. Kutscherauer), gregor.wehinger@kit.edu (G.D. Wehinger), Gerhard.Mestl@clariant.com (G. Mestl), turek@icvt.tu-clausthal.de (T. Turek).

Nomenclature

Latin symbols

b	Activity factor [-]
d	Diameter m
E_A	Activation energy [$\mathrm{kJ\,mol^{-1}}$]
$GHSV$	Gas-hourly-space-velocity [$\mathrm{m^3\,m^{-3}\,h^{-1}}$]
$\Delta_R H^0$	Reaction enthalpy [$\mathrm{kJ\,mol^{-1}}$]
k	Rate constant [misc.]
K	Equilibrium constant [misc.]
L	Length [m]
m	Number of data-points for Maximum Likelihood formulation [-]
N	Number of data-points for Maximum Likelihood formulation [-]
NE	Number of experiments for Maximum Likelihood formulation [-]
NM	Number of measurements for Maximum Likelihood formulation [-]
NV	Number of variables for Maximum Likelihood formulation [-]
R	Ideal gas constant [$\mathrm{J\,K^{-1}\,mol^{-1}}$]
r	Reaction rate [$\mathrm{mol\,kg^{-1}\,s^{-1}}$]
T	Temperature [°C or K]
t	Time [s]
TOS	Time on stream [h]
x	Molar fraction [mol %]
z	Predicted value for Maximum Likelihood formulation [misc.]
$\tilde{z}$	Predicted value for Maximum Likelihood formulation [misc.]

Greek symbols

α	Activity factor [-]
ε	Bulk content [-]
Θ	Surface coverage [-]
θ	Parameter set [-]

Abbreviations

1D	One-dimensional
CFD	Computational fluid dynamics
MA	Maleic anhydride
IR	Infrared
TEP	Tri-ethyl phosphate
TMP	Tri-methyl phosphate
VPO	Vanadium phosphorous oxide

Subscripts

ads	Adsorption
cat	Catalyst
des	Desorption
inert	Inert
P	Phosphorus
p	Particle
ref	Reference temperature (693 K)
SBT	Salt-bath-temperature

invoke a performance evolution of the VPO catalyst. This phenomenon is commonly referred to as *phosphorus dynamics*, where the catalyst experiences a loss of phosphorus leading to increased catalytic activity with decreased selectivity towards MA (Wilkinson et al., 2013; Lesser et al., 2016, 2017; Müller et al., 2022; Anderson et al., 2023b,a). Industrially, organophosphorus substances, such as tri-methyl-phosphate (TMP) or tri-ethyl-phosphate (TEP), are added to the feed stream (1 ppm to 3 ppm) to replace the lost phosphorus and maintain a constant level of

activity (Volta, 2000; Lesser et al., 2017; Müller et al., 2022; Wellauer et al., 1981; Ebner, 1993; Diedenhoven et al., 2012; Edwards, 1987, 1989; Taheri, 1992; Burnett et al., 2001). Further common issues with these reactor types lie in the inhomogeneous packing of reactor tubes, which leads to a distributed pressure drop over the entirety of tubes, and ultimately to variations in residence time per tube. Inhomogeneous salt-bath-temperatures, and temporal variations of water content in the compressed ambient air used for the reactor feed are also amongst those issues (Müller et al., 2022).

Considering the aforementioned challenges, it becomes readily apparent that precise reactor control is of utmost importance to maintain a high target product yield, and ensure safe and economic operation. Naturally, in-depth knowledge of the involved processes is a prerequisite for optimizing reactor control, comprising of several phenomena on different length scales, as visualized in Fig. 1. This reaches from the smallest length scale, the catalytic reaction and the phosphorus dynamics on a molecular level, over intra- and inter-particle heat and mass transport on a particle and tube level, to salt-bath cooling and distributed pressure drops on the entire reactor scale.

Often, classical measurement techniques fail to provide the full image: (Dixon, 2017) showed how local hot-spots, for example in the radial direction, are not captured by axial thermocouples placed in individual reactor tubes. Kutscherauer et al. (2024) showed how a single catalyst particle close to the reactor wall exhibited higher temperature and *n*-butane conversion than the remainder of the fixed-bed and Dong et al. (2018) reported temperature differences of up to 40 K on a single catalyst particle, both using computational fluid dynamics simulations (CFD). Using CFD simulations, too, Anderson et al. (2023a) reported that, under hot-spot conditions, a single VPO catalyst particle can experience temperatures of up to 80 K above the temperature of the surrounding bulk fluid, due to external heat transport limitations. Such effects would clearly not be recognized by an axial thermocouple measuring the gas phase temperature in the center of a reactor tube. The ability to describe the aforementioned processes in mathematical terms, independently of one another, can therefore be employed to close the knowledge-gap via modelling, ultimately leading to optimized control and operating policies for such reactors.

Throughout the past decades, a multitude of kinetic models has amassed in the literature: The earliest publications date back to the mid-1980s (Wellauer et al., 1986; Centi et al., 1985; Buchanan and Sundaresan, 1986), many publications around the early 2000s (Brandstädter and Kraushaar-Czarnetzki, 2005; Gascón et al., 2006; Lorences et al., 2003; Uihlein, 1993) and only a few models in recent years (Wilkinson et al., 2013; Lesser et al., 2017; Müller et al., 2021). These models differ in the type of reactor used to generate the kinetic data, the form of the rate expression and the type and complexity of the reaction network considered.

Unfortunately, only a few of these reaction kinetics also take the phosphorus dynamics into account (Anderson et al., 2023b). Wellauer et al. (1986) were among the first to model the selective oxidation of *n*-butane. Their publication from 1986 covers a reactor model, reaction kinetics and a deactivation model that is based on an Arrhenius expression, describing the deactivation of the catalyst by sublimation of phosphorus on the catalyst surface. Over 25 years later, Diedenhoven et al. (2012) brought the topic of the phosphorus dynamics back to life: they presented a hypothetical model for a reversible sorption process, that could be used to describe the phosphorus dynamics. However, they did not perform any experiments or attempt to parameterise the model. Another noteworthy study in this context is the work by Wilkinson et al. (2013), in which the transient change of catalytic activity during the conditioning phase of a fresh VPO catalyst is modelled using an activity-time approach. Although, strictly speaking, this is separate to the phosphorus dynamics, their transient description of catalytic activity makes this somewhat related. The most recent, and current state-of-the-art model on the phosphorus dynamics was published by Lesser et al. (2017) in 2017. It comprises of reaction
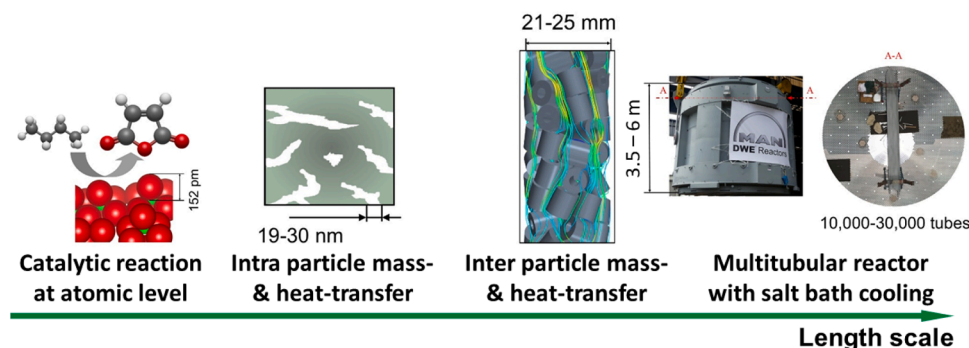
Fig. 1. Modelling an industrial MA reactor requires detailed description of phenomena taking place on several different length scales.

kinetics paired with a dynamic activity model for the phosphorus dynamics. Although it is able to describe the measured data with remarkable accuracy, its application is limited as a consequence of the model being derived from pilot reactor measurements, and hence including transport effects in the kinetic parameters, meaning that the model is strictly only valid for the parameter space it was fitted within. In an attempt to rectify this, Müller et al. (2021) published reaction kinetics from measurements in a μ-reactor, especially designed for measuring kinetic data for highly exothermic reactions under transport limitation-free conditions. However, their model only covers the reactions kinetics, and is as of yet lacking the transport limitation-free model for the phosphorus dynamics.

Further complicating this topic is the fact that little is known about the actual underlying physico-chemical mechanisms of the phosphorus dynamics, as evidenced by the lack of topical literature, and by the complicated surface chemistry of the VPO system. The catalyst surface is composed of a multitude of different VPO species (e.g. vanadyl pyrophosphate $(VO)_2P_2O_7$, different vanadyl phosphate phases α, γ, δ-VOPO$_4$), which contain Vanadium in different oxidation states (V^{3+}, V^{4+}, V^{5+}) (Badehbakhsh et al., 2023). Additionally, there are transient changes in surface composition taking place under reaction conditions. For example, Ihli et al. (2021) reports a change from a dark green-blue color to lint green for spent catalyst pellets, which is indicative of a shift from V^{4+} to V^{3+}. Further, a multitude of studies report a reduction of surface area for spent catalyst (Ihli et al., 2021; Badehbakhsh et al., 2023; Anderson et al., 2023b). Böcklein et al. (2017) found negative correlations between surface phosphorus content and catalytic activity, which they attributed to a reduction in concentration of active sites on the catalyst surface. Studies by Cavani et al. (2010a,b) report an influence of the P/V-ratio in the surface-near volumes of the catalyst on n-butane conversion and MA selectivity, further indicating that the phosphorus content of the surface plays a role in moderating the catalytic activity. A few other studies and patents indicate that water plays a role, too. It is suspected that steam aids in the distribution of phosphorus along the fixed-bed (Edwards, 1987, 1989; Burnett et al., 2001), and Anderson et al. (2023b) reported that steam in the reactor feed lowers the temperature at which the first signs of phosphorus loss can be observed. Clearly, the little knowledge available mostly reports observable effects, rather then hard evidence for a proposed mechanism. It is also unclear what happens to the selectivity-mediators TMP and TEP once they are dosed to the feed, whether or not they undergo chemical transformation before they reach the catalyst (Lesser et al., 2016, 2017; Anderson et al., 2023b).

In continuation of previous work on the phosphorus dynamics in the μ-reactor (Anderson et al., 2023b), we aim to develop a dynamic activity model, measured under heat and mass transport limitation-free conditions, to be coupled with the reaction kinetics by Müller et al. (2021). Ultimately, the goal is to describe all subprocesses independently and couple them, as shown in Fig. 1, to advance the design and optimization of industrial MA reactors. During the development of the model, it is the authors aim to maintain the descriptive equations as close to

actual physical phenomena as possible, in hopes of providing a better understanding of the phosphorus dynamics, in part or as a whole, along the way.

2. Experimental

2.1. Reactor

All experiments where conducted in a slit fixed-bed reactor (hereafter referred to as μ-reactor), originally developed by Hofmann and Turek (2017) and further improved by Müller et al. (2020a). A previous publication describes the experimental setup in detail (Anderson et al., 2023b), hence only a brief overview is given here.

The μ-reactor consists of two metal plates with a rectangular milled recess of $1.65\,mm$ on one of them, and is assembled by fixing both plates onto each other, fastening them with 16 M12x50 bolts, and thereby creating a space for the fixed-bed (see Fig. 2). Industrial VPO catalyst (Clariant SynDane ©, 97 % vandyl pyrophosphate $(VO)_2P_2O_7$ and 3 % graphite) was milled and sieved. Steatite particles (Mühlmeier GmbH & Co. KG, Bernau, Germany) were used as inert material for dilution of the catalyst, being sieved as well. In order to exclude mass transport limitations, based on the findings of Müller et al. (2020a), the $450\,\mu m$ to $630\,\mu m$ fraction of the catalyst were then used for the packing of the μ-fixed-bed. The same sieve fraction of the steatite particles was used. A molten salt bath (55/45 wt% KNO_3 / N_aNO_3) is used for precise temperature control of the submerged μ-reactor. A syringe pump (Fink Chem + Tec LSP01-1C) was used to dose liquid TMP (Merck $\geq 98\,\%$) at flow rates between $10\,nL\,h^{-1}$ and $1\mu Lh^{-1}$. After the μ-reactor, the product gas is stripped of condensable components in a series of stripping vessels, and dried via a cooling trap, before entering an IR Gas analyzer (Rosemount X-Stream) to measure the gas concentrations. N_2 is used as internal standard to obtain absolute flow rates from concentrations. It is assumed that all carbon that is not measured as n-butane, CO, or CO_2 at the IR-analyzer, is converted to MA. Quantities of other byproducts are usually insignificant, and are often neglected (Buchanan and Sundaresan, 1986; Schulz et al., 2018). The IR-analyzer is equipped with a paramagnetic cell to measure the oxygen concentration, which is used to calculate an oxygen balance, to verify this assumption. The error of the oxygen balance was within $\pm 2\,\%$, in all experiments. For a more detailed description the authors refer the avid reader to the previous publications by Hofmann and Turek (2017), Müller et al. (2020a,2020b,2021) and Anderson et al. (2023b).

2.2. Experimental

The relevant parameters for the phosphorus dynamics were determined as TMP concentration, salt-bath-temperature and feed water content. Hence, these parameters were varied throughout the μ-reactor experiments. The rather narrow range of investigated salt-bath-temperatures is a results of two constraining factors: In previous work (Anderson et al., 2023b) it was reported that onset of phosphorus loss
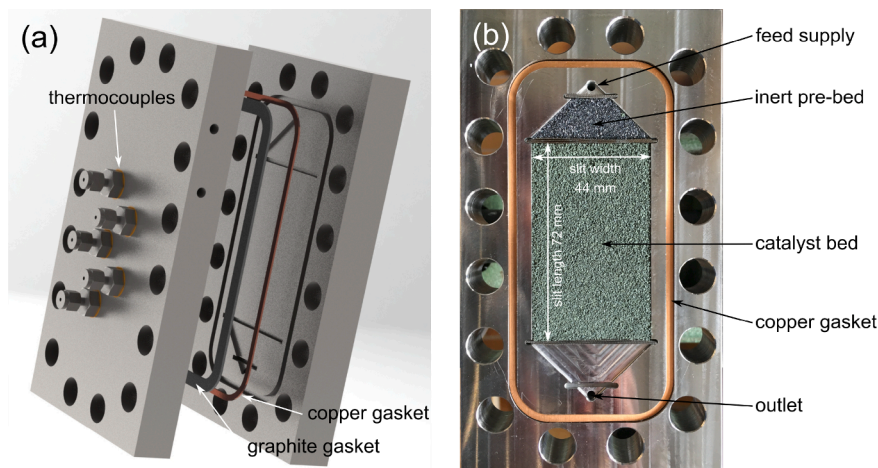
Fig. 2. The μ-reactor consists of two metal plates, where the fixed-bed is placed in a milled recess. Through crushed industrial catalyst particles and a high surface-to-volume ratio, heat and mass transport limitations are almost completely excluded (Müller et al., 2020a). © 2019 Müller et al. Published by WILEY-VCH Verlag GmbH & Co. KGaA, Weinheim.

Table 1
Overview of the experimental conditions investigated in this study.

T_{SBT}	X_{H_2O}	x_{TMP}	$GHSV$	m_{cat}	m_{inert}	$x_{C_4H_{10}}$	x_{O_2}
°C	mol %	mol-ppm	m³ m⁻³ h⁻¹	g	g	mol %	mol %
430	2	2	3200	3.997	2.402	1.5	20.265
410	2	2	2500	4.003	2.346	1.5	20.265
410	3	2	2500	4.003	2.346	1.5	20.055

was observed at 450 °C to 460 °C, depending on the feed steam content. To avoid a shift of the baseline catalytic activity throughout the duration of the experiments, the maximum temperature was limited to 430 °C, therefore. Since the composition for the fixed-bed was the same for all tested conditions, the contact time with the catalyst was modified according to the salt-bath-temperature, to maintain conversion levels close to industrially relevant conditions. This contact time modification is expressed in terms of the gas hourly space velocity ($GHSV$), and the required $GHSV$ values for each temperature were estimated with a steady state 1D-1D heterogeneous model, published by Müller et al. (2021). The minimum realizable flow rate of the μ-reactor setup imposes a lower limit of 410 °C to the salt-bath-temperature. Table 1 lists the values for each set of measured conditions. During previous experiments it was found that dry-feeding TMP did not invoke a discernible change of the catalytic activity. It is suspected that the entirety of the dosed phosphorus species binds to the first layers of the catalyst bed, such that the remainder of the catalyst does not come in contact with any phosphorus. Hence, only operating points with water added to the feed stream were investigated: 2 % and 3 %. Each combination of the varied parameters was tested twice, to ensure reproducible results.

In order to quantify the effect of phosphorus addition to the catalyst, experiments involving phosphorus dosing for a short period of time, followed by a subsequent period without phosphorus addition to the feed, were carried out. Once a steady state, characterised by stationary conversion and selectivities, was reached, TMP was dosed for a duration of 1 h. After 1 h, the phosphorus dosing was stopped and no further TMP was added to the feed. The μ-reactor was then operated without external disturbances, until the aforementioned metrics had reached a new steady state.

3. Model formulation

As global conversion in the kinetic experiments reached anywhere from 50 % to 70 %, the reactor is clearly operated in an integral man-

ner. Despite the fact that the reactor has been optimised for low influence of transport effects (Hofmann and Turek, 2017, Müller et al. 2020a,2020b,2021, Anderson et al., 2023b) the integral operation of the reactor necessitates the use of a reactor model to account for the considerable evolution of physical conditions along the length of the fixed-bed. The dynamic activity model describing the phosphorus dynamics does not cover the intrinsic reaction rates. Hence, reaction kinetics are required to describe the conversion of educts to products throughout the reactor. In the context of this study, the complete model thus comprises of a reactor model, a reaction kinetic model, and a dynamic activity model.

3.1. Reactor model

A steady state 1D-1D heterogeneous reactor model was used for this purpose. Due to the geometrically thin nature of the μ-fixed-bed (slit width 1.65 mm), it is assumed that radial gradients can be neglected (Müller et al., 2021). This carries a major advantage in terms of computational effort, especially when considering transient phenomena. The catalyst particles are modelled as spherical particles of diameter d_p, which equals the Sauter mean diameter of the real crushed particles. The Binary-Friction-Model (Ertl et al., 1997) is used to calculate the mass transport within the solid particles. The pressure drop created by the μ-fixed-bed is calculated according to Eisfeld and Schnitzlein (2001), Hofmann and Turek (2017). Since the model is one-dimensional, the heat transfer between the μ-fixed-bed and the reactor wall is described using an overall heat transfer coefficient according to Dixon (1996). Correlations from Zehner and Schlünder (1972), and Wellauer et al. (1981) are used to calculate the effective radial thermal conductivity of the catalyst bed and the bed to wall heat transfer coefficient used in the calculation of the effective heat transfer coefficient (Müller et al., 2021). More detailed information is available in the original publication of the model by Müller et al. (2021) and in the supporting information.

3.2. Reaction kinetics

Mars-van-Krevelen type rate equations are implemented into the reactor model to account for the reaction. More specifically, the reaction kinetic model published by Müller et al. (2021) is used, which is based on data measured in the same reactor configuration as used in this study.

These kinetics describe the consecutive reactions by using three separate active sites, each of which is assigned a specific part of the reaction
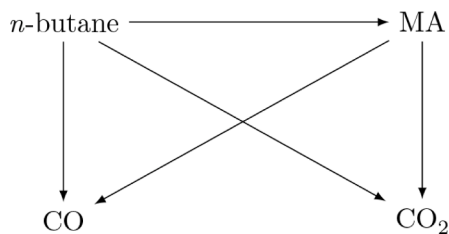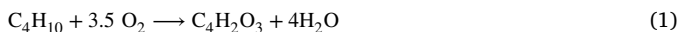
Fig. 3. Simplified four-species-five-reaction reaction network for the selective oxidation of *n*-butane to MA (adapted from Müller et al., 2021).
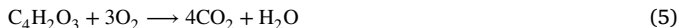
network (Fig. 3). Active site 1 (AS1) is responsible for the *n*-butane activation reaction:

$$C_4H_{10} + 3.5\ O_2 \longrightarrow C_4H_2O_3 + 4H_2O \tag{1}$$

$$C_4H_{10} + 4.5\ O_2 \longrightarrow 4CO + 5H_2O \tag{2}$$

$$C_4H_{10} + 6.5\ O_2 \longrightarrow 4CO_2 + 5H_2O \tag{3}$$

Further oxidation of MA to CO takes place on active site 2 (AS2):

$$C_4H_2O_3 + O_2 \longrightarrow 4CO + H_2O \tag{4}$$

Active site 3 (AS3) is responsible for the further oxidation of MA to CO_2:

$$C_4H_2O_3 + 3O_2 \longrightarrow 4CO_2 + H_2O \tag{5}$$

For the exact rate equations and more detailed information on the derivation of the reaction kinetics, the authors refer the avid reader to the original publication (Müller et al., 2021) and to the supporting information.

3.3. Dynamic activity model

Fig. 4 shows a schematic representation of the dynamic activity model, as it is developed in this work. Since it is not exactly known which form the dosed TMP assumes once it has entered the feed stream, it is assumed, that a not further defined phosphorus-species P, which is modelled after TMP, ad- and desorbs on the surface of the catalyst. The adsorption results in a fraction of the catalyst surface being covered by P.

Assuming that the spatial distribution of the active sites on the catalyst surface is homogeneous, i.e. there are no areas of pronounced high or low active site density, an equal fraction of each active site is blocked, and hence unavailable for reaction. The fraction of vacant active sites is then used to determine the level of activity of the catalyst, and to scale the reaction rates accordingly.

The rate of adsorption depends on a rate constant k_{ads}, the partial pressure of the hypothetical phosphorus species p_P and the fraction of vacant surfaces sites $1 - \Theta_P$. The desorption simply depends on a rate constant k_{des} and the fraction of occupied sites, expressed by the surface coverage Θ_P. Subtraction of those two terms from each other, yields the

time derivative of the surface coverage with phosphorus, Θ_P, as formulated in Eq. (6).

$$\frac{\partial \Theta_P}{\partial t} = k_{ads} \cdot p_P \cdot \left(1 - \Theta_P\right) - k_{des} \cdot \Theta_P \tag{6}$$

$$k = k_0 \cdot exp\left(-\frac{E_A}{R} \cdot \left(\frac{1}{T} - \frac{1}{T_{ref}}\right)\right)\Bigg|_{ads,des} \tag{7}$$

Temperature dependencies for rate constants are accounted for by using the Arrhenius law, see Eq. (7), and are related to a reference temperature of $T_{ref} = 693$ K. An activity factor $\alpha(\Theta_P)$, which essentially represents the fraction of non-phosphorus-blocked surface sites, is then calculated from the surface coverage via Eq. (8).

$$\alpha(\Theta_P) = 1 - \Theta_P \tag{8}$$

The activity factor is then introduced into the reaction kinetics, by multiplication with the steady state reaction rate expressions $r_{i,j}^0$. Essentially, $\alpha(\Theta_P)$ can be understood as a scaling factor, ranging anywhere from 0 to 1.

$$r_{i,j}(\Theta_P) = \alpha(\Theta_P) \cdot r_{i,j}^0 \tag{9}$$

Separate treatment of the reaction kinetics and the phosphorus dynamics is permissible, as the time scales at which both processes take place are separated by several orders of magnitude (Lesser et al., 2017). While changes affecting the reaction kinetics occur on a time scale of a few seconds, the phosphorus dynamics take place within hours, tens of minutes at best (Lesser et al., 2016, 2017; Anderson et al., 2023b). It is therefore a reasonable assumption that the reaction kinetics reach a steady state within the time frame of any transient changes caused by the phosphorus dynamics. This assumption allows to combine a steady state reactor model, steady state reaction kinetics and a transient dynamic activity model into an overall pseudo-transient model formulation.

Further, the hypothetical phosphorus species P must be included in the conservation equations of the reactor model. Diffusion inside of the porous catalyst is explicitly not considered, instead, it is assumed that the catalyst efficiency with regards to species P is equal to one: $\eta_{cat,P} = 1$. Justification for this lies once again in the time scales of the processes: A pore diffusion process is much faster, occurring within seconds rather than hours (Lesser et al., 2017).

From the description of the model, it follows that:
The changes in catalytic activity are fully reversible - once P has desorbed, and an active site is thus vacant, it is available for reaction again.
The changes in catalytic activity are unselective - a homogeneous distribution of all three active sites along the catalyst surface is assumed, such that all active sites are subject to the same fraction of surface coverage and thus site blocking.

This formulation of a dynamic activity model bears resemblance with the model proposed by Lesser et al. (2017). However, Lesser used the surface coverage to describe a change from an active site to a non-active site, via specific activity constants. The surface coverage is therefore not directly correlated to the catalytic activity. In contrast, our model
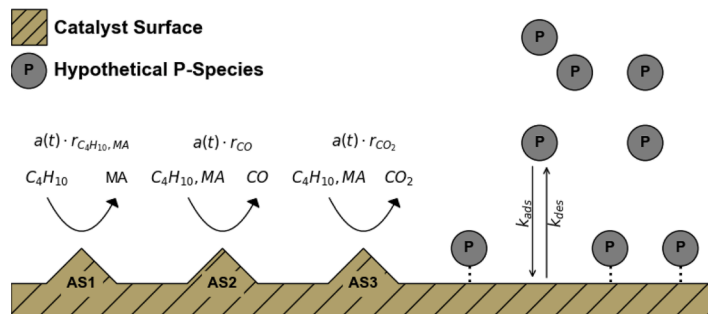

Fig. 4. A site-blocking mechanism is proposed to describe the deactivation of VPO catalyst through addition of tri-methyl phosphate to the feed stream.

Table 2

Results of the parameter estimation for the proposed site-blocking model.

Parameter	Value	Unit	SD
$k_{ads,0}$	1.85	$mol\,kg^{-1}\,bar^{-1}\,s^{-1}$	0.02
$k_{des,0}$	1.03E-5	$mol\,kg^{-1}\,s^{-1}$	2.12E-7
$E_{A,ads}$	44.78	$kJ\,mol^{-1}$	4.74
$E_{A,des}$	151.16	$kJ\,mol^{-1}$	8.14

The correlation matrix is available in the supporting information.

explicitly assumes that the composition of active sites does not change, and that the deactivating mechanism is a simply site-blocking adsorption process, hence the direct correlation of surface coverage and catalytic activity.

Model parameterisation: These parameters were fitted to experimental data, measured in the µ-reactor (see Section 2, data available in the supporting information). Since the model proposes an unselective deactivation mechanism, only the *n*-butane conversion was used for parameter estimation: By definition the selectivities should follow from the reaction kinetics. Parameter estimation was performed with the Model Validation tool in Siemens gPROMS Process (Version 2023.2.1) (Siemens Industry Software Limited, 2024). A Maximum Likelihood formulation is used by gPROMS to optimize the objective function shown in Eq. (10). The parameter estimation is structured into virtual experiments, that contain the measured data, thereby representing the real-world experiments. In Eq. (10), N is the total number of data points given for the estimation, Θ is the set of parameters to be estimated, NE is the number of experiments, NV_i is the number of variables on the ith experiment, NM_{ij} is the number of measurements of jth variable in the ith experiment. σ_{ijk}^2 is the variance of the kth measurement of variable j in experiment i. $\tilde{z}_{ijk}$ and z_{ijk} are the measured, and predicted value of variable j in experiment i, respectively.

$$\Phi = \frac{N}{2}ln(2\pi) + \frac{1}{2} \cdot min_\theta \left\{ \sum_{i=1}^{NE} \sum_{j=1}^{NV_i} \sum_{k=1}^{NM_{ij}} \left[ln(\sigma_{ijk}^2) + \frac{(\tilde{z}_{ijk} - z_{ijk})^2}{\sigma_{ijk}^2} \right] \right\} \quad (10)$$

The values obtained from the parameter estimation are shown in Table 2, together with their respective standard deviation (SD).

It was found that the reaction kinetics by Müller et al. (2021) predicted a more active catalyst than what was measured in the experiments. Expressed in a more tangible manner: the reaction kinetics systematically over-predicted the measured *n*-butane conversion, prior to adding any phosphorus to the catalyst. To account for this deviation between the measured catalytic activity and the prediction via the reaction kinetics, the *n*-butane conversion was corrected via a parallel shift. This was done as follows: When the catalyst showed steady state activity (*n*-butane conversion, MA and CO$_x$ selectivity), the deviation between the measured and the predicted *n*-butane conversion was determined. This was done prior to exposure to phosphorus, thereby making sure that no surface coverage via phosphorus had taken place. The correction factor ranged from 0.977 to 0.935, and therefore lies within the range of accuracy reported by the original publication on the reaction kinetics (Müller et al., 2021). This baseline-shift of activity was necessary for the numerical stability of the estimation routine (compare Eq. (10)), as otherwise the baseline deviation between measured and predicted values would have been greater than the activity variations evoked by the phosphorus dosing, which would have lead to a failure to estimate the model parameters. For the purpose of clarity, whenever scaled results are presented in this study, they are clearly marked as such.

4. Results and discussion

In the following paragraphs, the results of the short-term dosing experiments and the subsequent simulations are presented. Where applicable, measured data and predicted values are compared. The measured data were used to fit the model, in all cases. All experiments (see Table 1) were simulated with the parameter set shown in Table 2.

Fig. 5 shows the *n*-butane conversion over time on stream (TOS) for all six dosing experiments (a–f). Measured data is plotted with circular markers, the predicted trajectories are drawn as solid lines. As can be easily seen from Fig. 5, and as already mentioned in Section 3, there appears to be a systematic deviation between the measured and predicted data. For the sake of better comparability, a third trajectory was introduced. The scaled predicted trajectories are shown as a dashed line, and they are parallel shifted to match the initial measured values. Fig. 5a,d show trajectories for a salt-bath-temperature T_{SBT} of 430 °C, with a feed stream water content of 2 mol %. The measured values start at an initial *n*-butane conversion of 68.5 % and 67.9 % at 0 TOS, respectively. After TMP dosing, at 1 TOS, and a trailing time until approximately 6 TOS, the *n*-butane conversion reaches a minimum at 66.6 % and 65.9 %. Hence, at 6 TOS, the conversion begins to rise again. An asymptotic increase begins, and Fig. 5d reaches the original conversion level of 67.9 % at a time of approximately 62 TOS. In Fig. 5a, the measured data stops at 67.3 % at 20 TOS, before the initial steady state conversion is reached again.

Fig. 5b,e and c,f show trajectories for a salt-bath-temperature T_{SBT} of 410 °C, with 2 mol %, and 3 mol % water in the feed stream, respectively. At 2 mol % water content, the initial measured conversion is 57.5 % and 58 %, for the A and B run, respectively. Meanwhile it is slightly lower with 57.8 % and 57.4 % at 3 mol % water content, for the two repetitions, respectively. One might expect a significantly lower conversion, compared to the values at a salt-bath-temperature of 430 °C, but one needs to keep in mind that the contact time was modified to maintain conversion as constant as possible. In line with the observations made for the trajectory of *n*-butane conversion at $T_{SBT} = 430$ °C, a drop in conversion, followed by an asymptotic increase towards the initial level of conversion is visible in all cases. The minimum values of conversion, 56.2 % and 56 % for 2 mol % water content, and 56.1 % and 56 % for 3 mol % water content, are reached at approximately 10 TOS, and 7 TOS, respectively. In all four cases, at 150 TOS, the *n*-butane conversion has reached the initial conversion level, again.

The predicted values exceed the timeline of the measured values in all cases. This is due to time constraints in the experiments, where the individual dosing runs were not ran until the steady state achieved over several days of operation, but rather until the conversion reached its initial level again (Fig. 5a presents an exception, as the run was interrupted at 20 TOS).

Measurements and predicted results match in quality: The time at, and the amplitude with which the initial deactivation takes place around the first 10 TOS, as well as the subsequent activation period are well described by the model. However, the predicted results are parallel shifted to higher *n*-butane conversions than the measured results, within a range of 1 % to 4 %. This parallel shift does not change throughout the experiments, hinting at a systematic error. At a salt-bath-temperature of $T_{SBT} = 410$ °C, the measured data points appear to be superposed with increased noise, leading to a scattered appearance when compared to $T_{SBT} = 430$ °C. Yet, the predicted trajectories still lie within the slightly broader range of the measurements.

Fig. 6 shows measured and predicted values for selectivities with respect to the main products MA, CO, and CO$_2$ over time for the six dosing experiments. The repetitive runs are differentiated by color, where the first experiment (A-Run), is a light grey, and the second experiment (B-Run), is a dark grey. In all cases shown, selectivity is highest towards MA, followed by CO and then CO$_2$. For the two experiments at a salt-bath-temperature of 430 °C, the measured MA selectivity starts at 74.1 % and 73.9 %, respectively. It then increases by 0.4 % and 0.6 %, respectively, until 6 TOS and subsequently reduces again. For the A-run, the measured data stops at 20 TOS with a MA selectivity of 74.2 %. The B-run reaches a MA selectivity of 74.0 % at approximately 60 TOS, which coincides with the initial level of selectivity. The selectivities with respect to CO and CO$_2$ show an inverse behaviour: While for the A-run, they start at 15.4 % and 10.5 %, followed by a reduction of 0.1 % and 0.2 % until 6 TOS, and they subsequently increase again until the measured
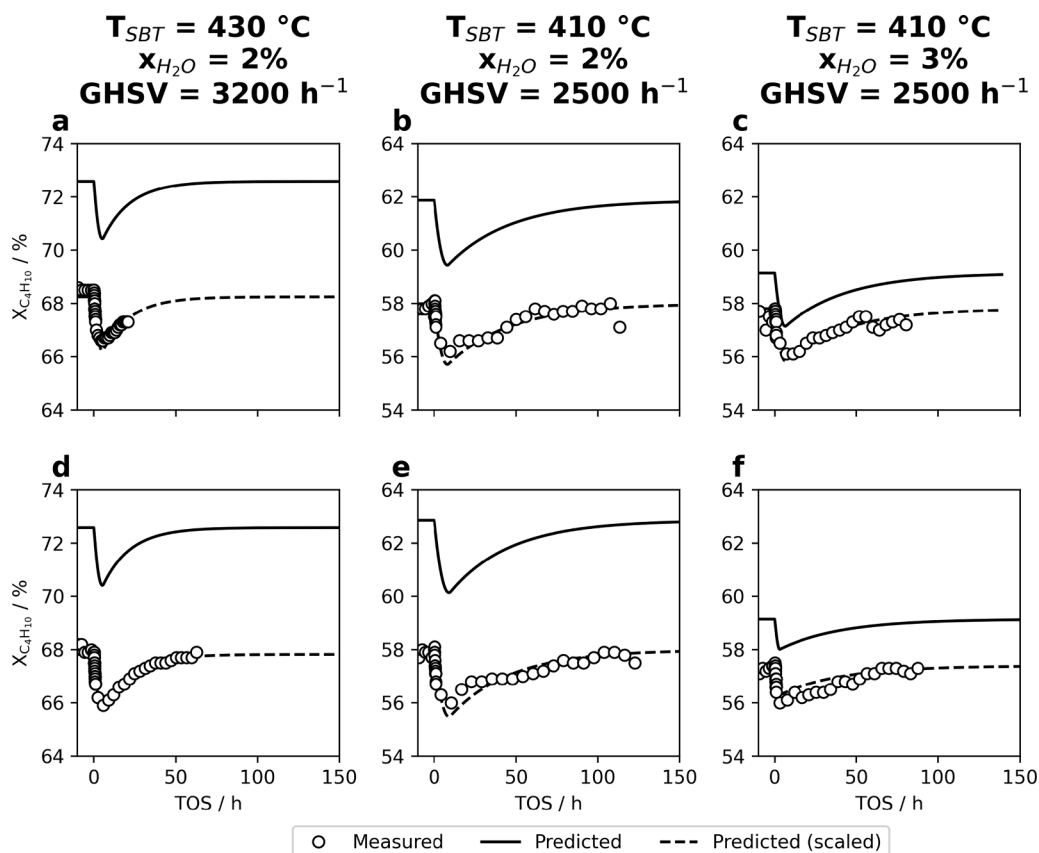
Fig. 5. Measured (data-points), predicted (solid line), and corrected for the initial intrinsic activity (dashed line) results for *n*-butane conversion over time-on-stream for the six phosphorus dosing experiments are shown.

data stops at 20 TOS. For the repetition run, CO and CO_2 selectivities start at 15.5 % and 10.5 %, drop to 15.2 % and 10.3 % at the 6 TOS mark, and subsequently increase until they reach 15.5 % and 10.5 % at 60 TOS, respectively. Fig. 6b,c,e,f,h,i all show similar behaviour to the previously described cases, with a parallel shift, as already observed with the conversion in Fig. 5. In the case of the MA selectivity S_{MA}, the predicted values are slightly below the measured values, with all cases being in the range of 2.6 % to 2.8 %. In case of CO and CO_2, the predicted selectivities exceed the measured values, within a range of 0.7 % to 1.2 % and 1.4 % to 1.6 %, respectively.

For the lower salt-bath-temperature of 410 °C, the selectivities exhibit a similar temporal evolution, but their baseline values are slightly shifted compared to 430 °C: The measured MA selectivity is slightly higher, at approximately 78 %, while CO and CO_2 are slightly lower at approximately 13 % and 9 %. For the different water contents, no difference in selectivity can be interpreted from Fig. 6. The predicted values show the same behaviour as for $T_{SBT} = 430$ °C.

Fig. 7 shows values for the surface coverage and the resulting activity factor, along the lengthwise axis (z-axis) of the μ-reactor over time, for two selected experiments (Fig. 7a,b: $T_{SBT} = 430$ °C and $x_{H_2O} = 2$ % - B Run, and Fig. 7c,d: $T_{SBT} = 410$ °C and $x_{H_2O} = 2$ % - A Run). As the surface coverage along the reactor cannot be measured, and the activity factor $a(\Theta_P)$ is a purely mathematical quantity that does not bear any physical basis, these values are purely predicted, i.e. they are computed from the model. The value of the surface coverage Θ_P and the activity factor $a(\Theta_P)$ are indicated by the color bar to the left of each plot. For the purpose of clarity, the time was limited to 100 TOS. Fig. 7a shows a surface coverage of $\Theta_P = 0$ at 0 TOS, over the entire reactor length. Correspondingly, the activity factor $a(\Theta_P)$ is 1 (see Fig. 7b). At approximately 6 TOS, 5.1 % of the surface is covered with phosphorus ($\Theta_P = 0.051$ and $a(\Theta_P) = 0.949$). From there on, the surface coverage de-

creases again. At 18 TOS, the surface coverage has halved to 2.5 %, and the activity factor is 0.975. At 45 TOS, only 0.5 % are covered, with an activity factor of 0.995. A completely vacant surface, corresponding to $\Theta_P = 0$ and $a(\Theta_P) = 1$ is reached at around 75 TOS. At no time is there any gradient visible over the length of the μ-reactor.

Fig. 7c,d show a similar behaviour until the maximum surface coverage and minimum activity factor is reached: From $\Theta_P = 0$ and $a(\Theta_P) = 1$ at 0 TOS, to $\Theta_P = 0.06$ and $a(\Theta_P) = 0.94$ at 8 TOS, the initially fully vacant surface is covered with phosphorus. After 8 TOS and onward, the phosphorus coverage reduces, and the activity increases: At 42 TOS, the surface is covered by only 2.5 %, and the activity factor is 0.975. A surface coverage of 0.5 % is reached at 104 TOS, corresponding to an activity factor of 0.995. A completely free surface, corresponding to $\Theta_P = 0$ and $a(\Theta_P) = 1$ is reached at around 166 TOS (not shown in Fig. 7c,d).

Fig. 8 shows parity plots for the *n*-butane conversion values for each of the six experiments. Measured values are shown on the x-axis, whereas predicted values are shown on the y-axis. A grey background indicates the ±1 % error interval, and the identity line is drawn as a dashed line. Fig. 8a,d, representing the two experiments at 430 °C, shows almost all data points can be found within 1 % of the identity line, indicating a remarkably accurate representation of the measured values by the model. For the experiments conducted at $T_{SBT} = 410$ °C, that is Fig. 8b,c,e,f, the predicted values by the model coincide less well with the measured values. Further, a more pronounced scatter of the markers can be observed, compared to Fig. 8a,d. However, despite the slightly increased scatter in the data, the majority of points still falls within 1 % of identity.

The agreement between predicted and measured values is remarkably high: Spatio-temporal trajectories are well described, only a few measured data points do not match the predicted values. However, these outliers can be attributed to experimental errors, rather than any
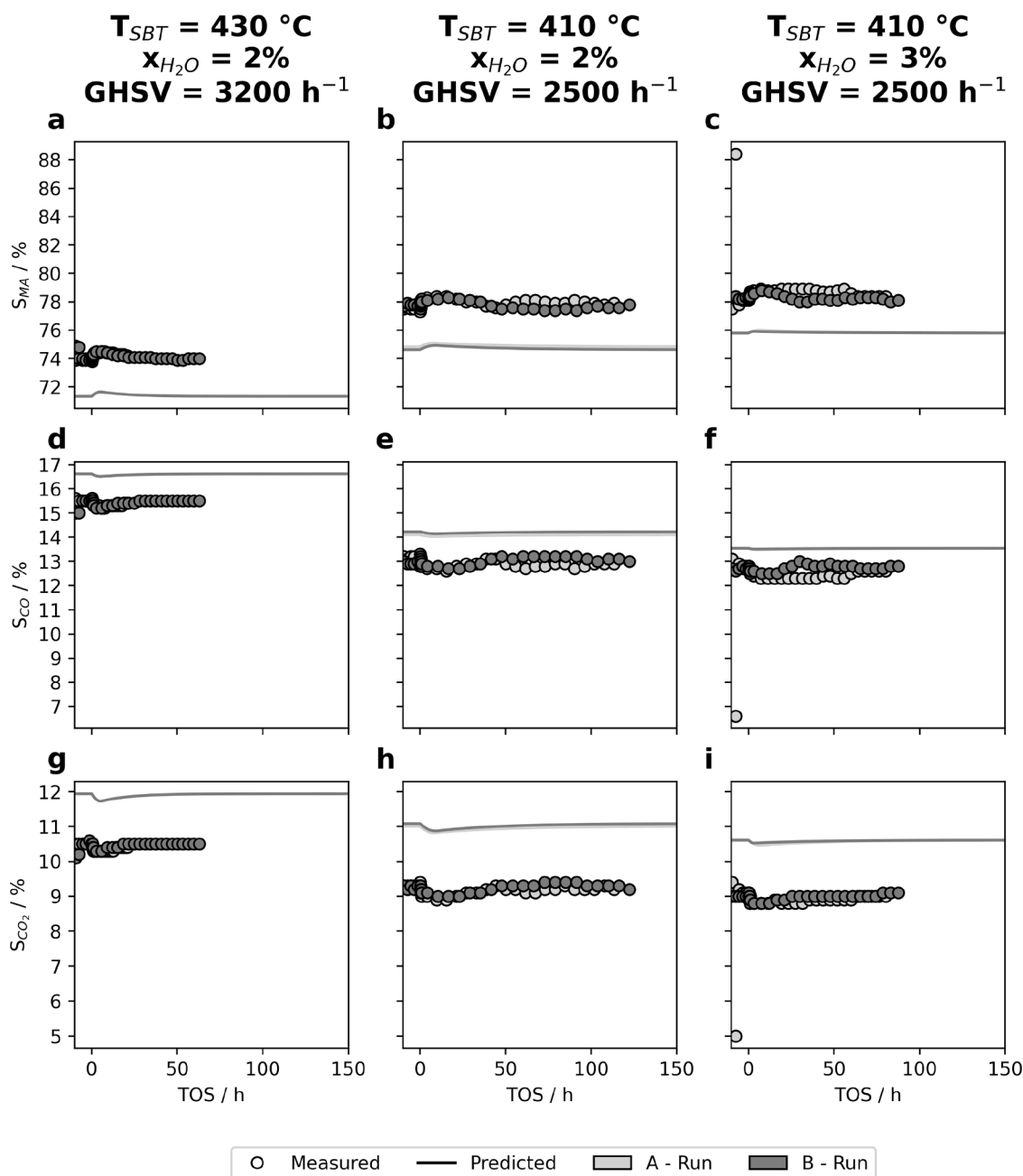
Fig. 6. Measured (data-points), and predicted (solid line) results for the selectivities during the phosphorus dosing experiments. Repetition runs are differentiated by color.

physical phenomena, and hence are not pertinent to the quality of the fit. The overall very good agreement between measured and predicted values is further reflected by the parity plots. An increased data scatter observed at $T_{SBT} = 410\,°C$, is easily explained by the contact time modification. For a lower $GHSV$, the absolute flow rates must be decreased, moving closer to the minimum values of all equipment. Thus, the relative impact of the error of said equipment is much higher, resulting in the increased data scatter at low flow rates. As mentioned earlier, the initial *n*-butane conversion, predicted by the reaction kinetics, had to be parallel-shifted to match the measured values. The predicted and measured selectivities also show this parallel shift. Throughout all of the respective dosing experiments, the deviation between reaction kinetics and measured values remained constant. In total, the deviation can be summed up as: The used reaction kinetics overestimate the catalytic ac-

tivity slightly, which leads to overestimated *n*-butane conversion, thus favouring the consecutive oxidation of MA, which leads to underestimated selectivity towards MA, and overestimated selectivities towards CO, and CO_2. This systematic deviation can be explained by two factors: The reaction kinetics by Müller et al. (2021) do not consider a diluted catalyst bed, as used in this study, and a different charge of the SynDane© catalyst was used for preparation of the µ-catalyst. Further, the reaction kinetics itself will have an intrinsic inaccuracy. For their final model, Müller et al. (2021) report parity plots for measured and predicted concentrations, where predicted values lie within $\pm 10\,\%$ of measurements. At low *n*-butane concentrations ($x_{C_4H_{10}} < 1\,\%$), deviations from the identity line are especially pronounced. In this study, measured *n*-butane concentrations were consistently below $1\,\%$, mostly even below $0.5\,\%$, due to the specification of high conversions made earlier.
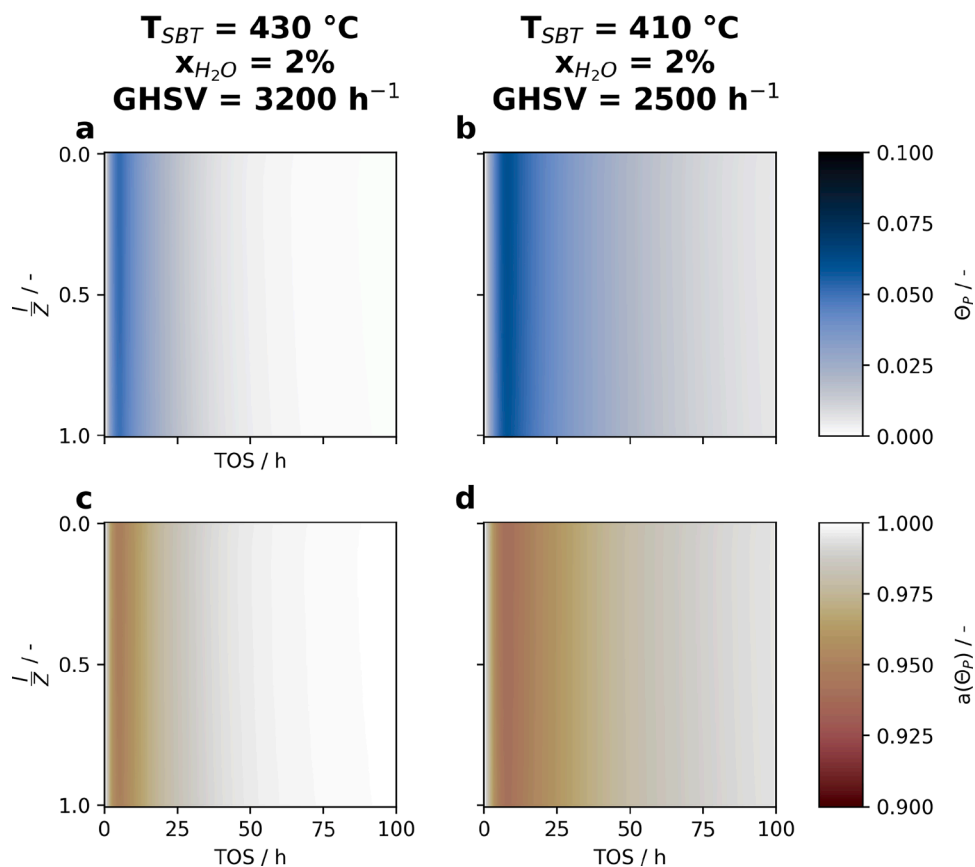
Fig. 7. Phosphorus surface coverage Θ_P and activity factor $\alpha(\Theta_P)$ plotted over time-on-stream and the axial reactor coordinate.
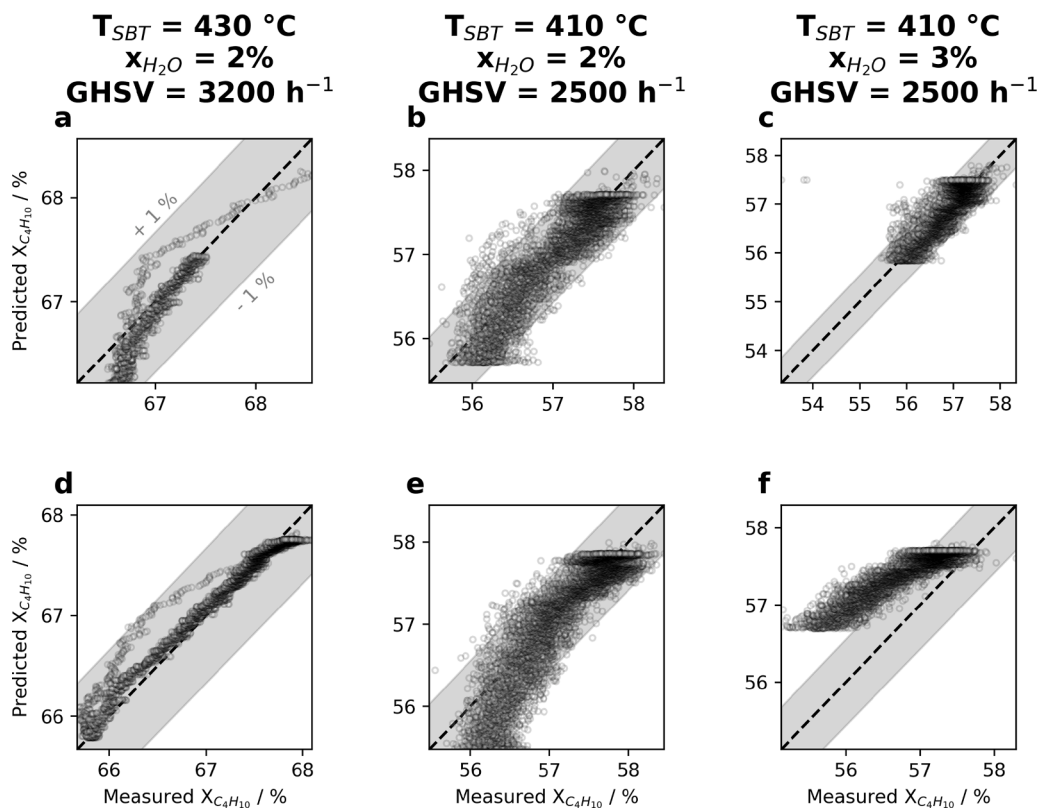

Fig. 8. Parity plot for measured and predicted *n*-butane conversion for all six phosphorus dosing experiments. Measured values are shown on the x-axis, whereas predicted values are shown on the y-axis. A grey background indicates the $\pm 1\%$ error interval, and the identity line is drawn as a dashed line.

With this in mind, the systematic deviation of $\Delta X_{C_4H_{10}} < 4\%$ between reaction kinetics and measured values can not only be explained, but also justified.

When comparing the selectivities shown in Fig. 6, it becomes apparent that a higher MA selectivity S_{MA}, and a lower oxidation to CO, CO_2 is achieved when lowering the salt-bath-temperature T_{SBT}. It is well known that the formation of CO and CO_2 have higher activation energies than the *n*-butane activation reaction. Consequentially, a lower temperature will result in a slightly decreased CO and CO_2 selectivity and slightly increased MA selectivity.

From the results described above, the following deductions can be drawn about the phosphorus dynamics:

The deactivation mechanism is reversible: Fig. 5 clearly shows how the conversion returns to its initial value post phosphorus dosing, and no permanent decrease in catalytic activity can be seen. Further, the proposed model is able to exactly describe the trajectories of the *n*-butane conversion. This in and of itself is an indicator that the effect is reversible, since by definition of the underlying ad-/desorption process that the model relies upon, is reversible.

The deactivation mechanism is unselective: Coinciding with the drop in conversion, the selectivities change as well (compare Fig. 6). Considering the reaction network shown in Fig. 3, it becomes apparent that MA is consecutively oxidized to CO, CO_2. A decrease in *n*-butane conversion thus means that the rate of consecutive oxidation is reduced, too, since the respective reaction rates depend on the partial pressure of MA (Müller et al., 2020b; Müller et al., 2021), thus leading to reduced selectivities with respect to CO, CO_2, while the MA selectivity increases. Theoretically, the shift in selectivities could be explained by a change in temperature, since the consecutive oxidation reactions have a higher activation energy than the *n*-butane activation reaction. However, the measured temperatures along the µ-fixed-bed change less than 1 K throughout the experiments, and the model does not report any significant changes of temperature either. The fact that the model is able to describe the observed changes in selectivity, despite the measured selectivities not being used as fit-data, is further evidence that the deactivation effect is unselective and these changes are merely a product of consecutive oxidation. Since the model features unselective deactivation by definition, yet is still able to describe the temporal change of selectivities, the observed deactivation effect must be unselective, as well.

Catalyst deactivation is faster then re-activation: Comparing the rate constants for the adsorption of the hypothetical phosphorus species P on the catalyst surface, which corresponds to the deactivation of the catalyst, to the rate constant for the desorption (activation/re-activation) reveals that the deactivation proceeds much faster (compare Table 2). $k_{ads,0}$ exceeds $k_{des,0}$ by five orders of magnitude. This reflects in Fig. 5, where the return to the initial level of *n*-butane conversion takes much longer than the drop of conversion in the first few hours. It has to be noted, that the proposed model is intended to describe macroscopic effects, such as the measured end-of-pipe quantities (*n*-butane conversion, product selectivities) that is was fitted to. It is neither intended, nor able to describe the intricate processes that may take place at the catalyst surface level. Hence, no conclusions on the actual physicochemical background can be drawn from this work. Instead, designated surface science studies should be conducted to tackle this question.

Increased temperatures favour the re-activation: The activation energy for the desorption $E_{A,des}$ of P exceeds $E_{A,ads}$ more than threefold, indicating that the desorption process exhibits a stronger temperature dependency than the adsorption. Comparing the trajectories for $T_{SBT} = 430\ °C$ and $T_{SBT} = 410\ °C$ in Fig. 5 reveals a less steep increase in conversion for the lower temperatures, and hence is in line with previous statements. Similarly, Fig. 7 shows how at lower temperatures, the surface coverage of the catalyst in the µ-fixed-bed reduces more slowly, compared to the higher temperature.

In summary, the data measured in the short-term dosing experiments confirms the hypothesized model and the consequential deductions for

the mechanism of the phosphorus dynamics. It appears as though a site-blocking mechanism through the addition of phosphorus containing species, such as TMP or TEP, to the reactor feed exists and plays a role in the phosphorus dynamics. However, it remains unclear if this model is exhaustive in describing the phenomenon of the phosphorus dynamics, or if further processes in the catalyst may play a role.

Considering the little knowledge available to date, several shortcomings of the model come to mind. First and foremost, it is well established that the VPO catalyst can undergo a permanent increase in catalytic activity. In an earlier publication (Anderson et al., 2023b), we showed that exposure to salt-bath-temperatures $T_{SBT} \geq 450\ °C$ leads to a permanent increase of conversion, and decrease of MA selectivity. Other researchers have found further evidence supporting this observation: Ihli et al. (2021) analyzed spent industrial catalyst taken from the hot-spot and the center region of an industrial MA reactor. They reported more changes in composition of VPO species, compared to pristine catalyst, with particles from the hot-spot showing more intense changes than particles from the center. This observation cannot be described by site-blocking, as in the model proposed within this work, since in that case the maximum reachable activity corresponds to an entirely vacant surface, i.e. $\Theta_P = 0$ and $a(\Theta_P) = 1$. Hence, it appears as though at least one additional mechanism must play a role within the phosphorus dynamics.

Further, it has been reported in the patent literature that steam plays an important role in the distribution of phosphorus along the fixed-bed (Edwards, 1987, 1989; Burnett et al., 2001). Lesser et al. (2016, 2017) report an influence of water on the phosphorus dynamics through competitive adsorption with phosphorus. In an earlier study (Anderson et al., 2023b), we report that addition of water to the reactor feed stream lowers the salt-bath-temperature required to invoke a permanent increase in catalytic activity. However, the measured data presented in this study do not reveal any influence of water on the phosphorus dynamics. This could well be a result of the comparably small range of feed steam content investigated (2 mol % and 3 mol %), which may not be a wide enough range to invoke measurable differences. Further, the steam content was varied at the lower of the two investigated salt-bath-temperature, where we reported increased data scatter due to the low absolute flow rates. In addition to the rather small difference in investigated steam content, it may be conceivable that the impact of the steam content falls within the order of magnitude of experimental error, and thus, despite its existence, may not be visible in the experiments presented herein.

5. Conclusion

In the present study, experimental results and a parameterised model have indicated that a site-blocking effect takes place through phosphorus as activity mediator on VPO catalysts. This effect has not yet been described in the literature, and to the best of the authors knowledge, fully reversible sorption of TMP on the VPO catalyst in the context of the phosphorus dynamics has not yet been reported, at all. Expanding on earlier work of our research group, this study presents the first application of phosphorus dosing under well-defined, limitation-free conditions in a fixed-bed reactor. The proposed and parameterised model is able to describe the measured results with remarkable accuracy, utilizing only four parameters and without having to introduce additional, non-physical parameters to improve the quality of the fit.

It appears as though the proposed site-blocking mechanism definitively plays a role in, but can not exhaustively explain, the phosphorus dynamics. There remain known effects that are not captured by the site-blocking model, such as permanent changes in catalytic activity, changes in the composition of the surface and thus the product selectivities, and the influence of water on the phosphorus dynamics. To address these observations, the authors propose an extension to the model presented within this study, which is schematically shown in Fig. 9: An additional quantity ε_P is introduced, describing the phosphorus content
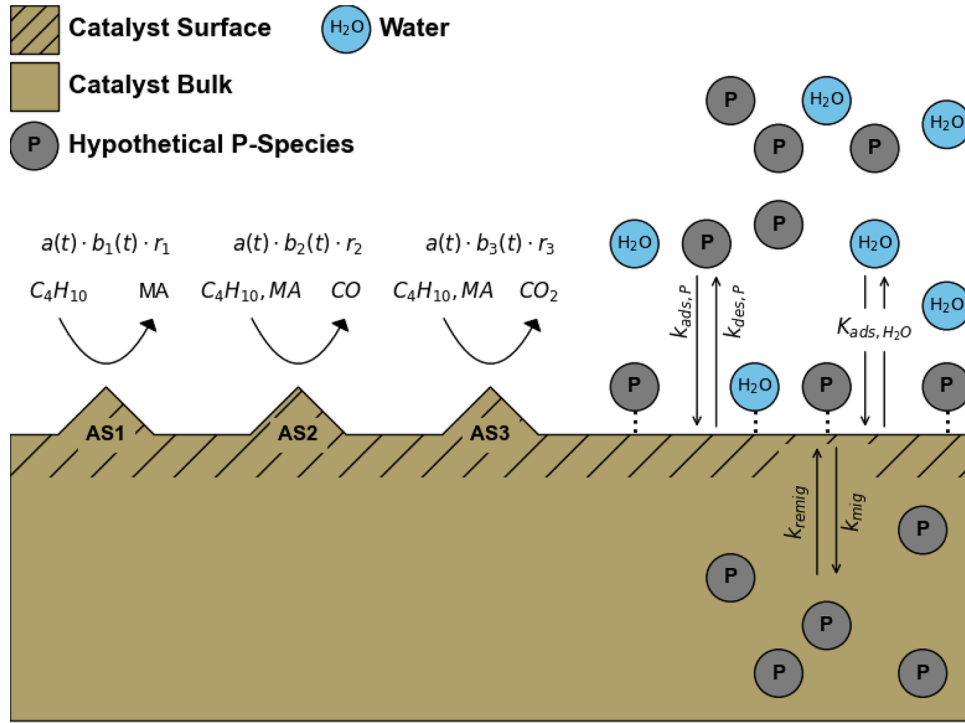
Fig. 9. Expanded model scheme, now accounting for a permanent change in catalyst phosphorus content, changes in surface composition and the influence of water.

of the surface-near volume of the catalyst. The phosphorus adsorbed on the surface can then either desorb, or migrate into the surface-proximal layers of the catalyst. Further, phosphorus from these surface-proximal layers can also migrate back toward the surface. This is described by introducing the derivative with respect to time of the phosphorus content ϵ_P into the sorption Eq. (6), thereby yielding Eq. (11). The time derivative of the phosphorus content ϵ_P is obtained via Eq. (12), where the migration in- and out of the surface-near volume is described in dependence of two rate constants that follow an Arrhenius approach (compare Eq. (7)), the surface coverage with phosphorus Θ_P, and the phosphorus content ϵ_P itself.

The influence of water is described with an equilibrium formulation, based on the assumption that water adsorption process is much faster compared to phosphorus (Lesser et al., 2017). This is mathematically expressed by incorporating the adsorption equilibrium constant K_{ads,H_2O} into the formulation of the fraction of vacant sites in Eq. (11).

From the phosphorus content ϵ_P, and a correlating factor k_b, a second activity factor b is calculated, as shown in Eq. (14). Since the phosphorus content of the surface-near volume is representative of the composition of the surface and the surface-proximal layers of the catalyst, a correlating factor k_b exists for each of the three active site of the reaction kinetics by Müller et al. (2021), and consequentially three activity factors $b(\epsilon_P)$ exist, too. Similar to the original model, the individual reaction rates are then scaled by the activity factor $a(\Theta_P)$, which is the same for all active sites, as it describes the unselective deactivation through site-blocking. The activity factor $b(\epsilon_P)$, depending on the active site the reaction is assigned to, describes the selective deactivation through permanent changes of the catalyst composition (see Eq. (15)). It has to be strictly differentiated between the product selectivity (e.g. S_{MA}) and the selective/unselective deactivation of the catalyst. Even during unselective deactivation, the product selectivities may be affected due to the consecutive reactions in the reaction network.

$$\frac{\partial \Theta_P}{\partial t} = k_{ads} \cdot p_P \cdot \frac{1 - \Theta_P}{1 + K_{ads,H_2O} \cdot p_{H_2O}} - k_{des} \cdot \Theta_P - \frac{\partial \epsilon_P}{\partial t} \quad (11)$$

$$\frac{\partial \epsilon_P}{\partial t} = k_{mig,in} \cdot \Theta_P \cdot (1 - \epsilon_P) - k_{mig,out} \cdot \epsilon_P \quad (12)$$

$$\alpha(\Theta_P) = 1 - \Theta_P \quad (13)$$

$$b_k(\epsilon_P) = k_{b,k} \cdot (1 - \epsilon_P)\big|_{k=1,2,3} \quad (14)$$

$$r_{i,j}(\Theta_P, \epsilon_P) = \alpha(\Theta_P) \cdot b_i(\epsilon_P) \cdot r_{i,j}^0\big|_{k=1,2,3} \quad (15)$$

Arising from this expansion of the proposed model, further research must be directed at short-term dosing experiments including a broader range of feed steam contents to shed light on the influence of water on the adsorption of phosphorus on the catalyst surface. Equally important, yet more complicated, measurements for the parameterisation of the migration term in and out of the surface-near volumes of the catalyst are required. This will be especially challenging, since no recurring baseline activity will ensue, necessitating well thought-through experimental approaches. Such experiments will most likely take a not insignificant amount of time, as the phosphorus loss, especially from deeper volumes of the catalyst bulk, is a comparably slow process taking place over several days or even weeks, thus adding more difficulties for the experimentor. Since the proposed expansion adds between eight to eleven parameters (depending on which constants are considered with temperature dependence) to the model, significantly more measurements are required for a high quality parameter estimation, and as the involved processes can not easily be separated experimentally, the risk for correlation of the parameter estimates increases, too. Further, the measurement of additional operating points should be considered, in order to validate the model with data that has not been used in the parameter estimation.

Parallel to the advancement of modelling the phosphorus dynamics, attention should be paid to closing the gap between macro-kinetic studies such as this one, and the actual physico-chemical processes taking place on the surface, and in surface-near regions of the catalyst, such as to combine both into an advanced understanding of the phosphorus dynamics.

Data availability

Data will be made available on request.

Declaration of competing interest

The authors declare that they have no known competing financial interests or personal relationships that could have appeared to influence the work reported in this paper.

CRediT authorship contribution statement

Scott D. Anderson: Conceptualization, Methodology, Investigation, Formal analysis, Validation, Writing - original draft, Writing - review & editing, Visualization, Project administration; **Martin Kutscherauer:** Conceptualization, Methodology, Formal analysis, Validation, Writing - review & editing; **Gregor D. Wehinger:** Supervision; **Gerhard Mestl:** Writing - review & editing, Supervision, Resources; **Thomas Turek:** Resources, Writing - review & editing, Supervision.

Funding

Supplementary material

Supplementary material associated with this article can be found in the online version at 10.1016/j.ces.2025.121880.

References

Anderson, S.D., Kutscherauer, M., Böcklein, S., Mestl, G., Turek, T., Wehinger, G.D., 2023a. Investigating the accuracy of continuum models for the simulation of industrial maleic anhydride reactors: a comparative single particle CFD study. Chem. Eng. Res. Des. 200, 655–669. https://doi.org/10.1016/j.cherd.2023.11.018

Anderson, S.D., Kutscherauer, M., Nickel, N., Böcklein, S., Mestl, G., Wehinger, G.D., Turek, T., 2023b. Phosphorus dosing during catalytic *n*-butane oxidation in a *μ*-reactor: a proof of concept. Ind. Eng. Chem. Res. 62 (47), 20142–20151. https://doi.org/10.1021/acs.iecr.3c02604

Badehbakhsh, S., Saadatkhah, N., Mahboub, M. J.D., Guerrero-Pérez, O., Patience, G.S., 2023. Morphological changes of vanadyl pyrophosphate due to thermal excursions. Catal. Today 407, 301–311. https://doi.org/10.1016/j.cattod.2021.12.008

Ballarini, N., Cavani, F., Cortelli, C., Ligi, S., Pierelli, F., Trifiro, F., Fumagalli, C., Mazzoni, G., Monti, T., 2006. VPO Catalyst for *n*-butane oxidation to maleic anhydride: a goal achieved, or a still open challenge? Top. Catal. 38 (1–3), 147–156. https://doi.org/10.1007/s11244-006-0080-z

Bartley, J.K., Dummer, N.F., Hutchings, G.J., 2008. Vanadium Phosphate Catalysts. John Wiley & Sons, Ltd. chapter 12. pp. 499–537. https://doi.org/10.1002/9783527626113.ch12

Böcklein, S., Mestl, G., Auras, S.V., Wintterlin, J., 2017. On the correlation of structure and catalytic performance of VPO catalysts. Top. Catal. 60, 1682–1697. https://doi.org/10.1007/s11244-017-0847-4

Brandstädter, W.M., Kraushaar-Czarnetzki, B., 2005. Maleic anhydride from mixtures of *n*–butenes and *n*-butane: effective reaction kinetics. Ind. Eng. Chem. Res. 44 (15), 5550–5559. https://doi.org/10.1021/ie050099o

Buchanan, J.S., Sundaresan, S., 1986. Kinetics and redox properties of vanadium phosphate catalysts for butane oxidation. Appl. Catal. 26, 211–226. https://doi.org/10.1016/S0166-9834(00)82553-1

Burnett, J.C., Alumbaugh, W.H., Reeves, L.A., 2001. Method and apparatus for improving the uniformity of distribution of a phosphorus-containing agent throughout a maleic anhydride catalytic reactor. US Patent 6300505.

Cavani, F., De Santi, D., Luciani, S., Löfberg, A., Bordes-Richard, E., Cortelli, C., Leanza, R., 2010a. Transient reactivity of vanadyl pyrophosphate, the catalyst for *n*-butane oxidation to maleic anhydride, in response to in-situ treatments. Appl. Catal. A Gen. 376 (1–2), 66–75. https://doi.org/10.1016/j.apcata.2009.10.037

Cavani, F., Luciani, S., Esposti, E.D., Cortelli, C., Leanza, R., 2010b. Surface dynamics of a vanadyl pyrophosphate catalyst for *n*-butane oxidation to maleic anhydride: an in situ raman and reactivity study of the effect of the P/V atomic ratio. Chem. Eur. J. 16 (5), 1646–1655. https://doi.org/10.1002/chem.200902017

Centi, G., Fornasari, G., Trifiro, F., 1985. *n*-butane oxidation to maleic anhydride on vanadium-phosphorus oxides: kinetic analysis with a tubular flow stacked-pellet reactor. Ind. Eng. Chem. Prod. Res. Dev. 24 (1), 32–37. https://doi.org/10.1021/i300017a007

Dammak, M., Fourati, Y., Tarrés, Q., Delgado-Aguilar, M., Mutjé, P., Boufi, S., 2020. Blends of PBAT with plasticized starch for packaging applications: mechanical properties, rheological behaviour and biodegradability. Ind. Crops. Prod. 144, 112061. https://doi.org/10.1016/j.indcrop.2019.112061

Denny, J., 2024. Maleic anhydride markets: an assessment for 2024. Retrieved 2025-04-10. https://www.resourcewise.com/blog/chemicals-blog/maleic-anhydride-markets-an-assessment-for-2024.

Diedenhoven, J., Reitzmann, A., Mestl, G., Turek, T., 2012. A model for the phosphorus dynamics of VPO catalysts during the selective oxidation of *n*-butane to maleic anhydride in a tubular reactor. Chem. Ing. Tech. 84 (4), 517–523. https://doi.org/10.1002/cite.201100248

Dixon, A.G., 1996. An improved equation for the overall heat transfer coefficient in packed beds. Chem. Eng. Process. 35 (5), 323–331. https://doi.org/10.1016/0255-2701(96)80012-2

Dixon, A.G., 2017. Local transport and reaction rates in a fixed bed reactor tube: endothermic steam methane reforming. Chem. Eng. Sci. 168, 156–177. https://doi.org/10.1016/j.ces.2017.04.039

Dong, Y., Geske, M., Korup, O., Ellenfeld, N., Rosowski, F., Dobner, C., Horn, R., 2018. What happens in a catalytic fixed-bed reactor for *n*-butane oxidation to maleic anhydride? Insights from spatial profile measurements and particle resolved CFD simulations. Chem. Eng. J. 350, 799–811. https://doi.org/10.1016/j.cej.2018.05.192

Ebner, J.R., 1993. Method for improving the performance of VPO catalysts. US Patent 5185455 A.

Edwards, R., 1987. Process for Improving Phosphorus-Vanadium Oxide and Phosphorus-Vanadium-Co-Metal Oxide Catalysts. US Patent 4701433.

Edwards, R., 1989. Process for Regenerating and Stabilizing Phosphorus-Vanadium-Oxygen Complex Catalysts. US Patent 4861738.

Eisfeld, B., Schnitzlein, K., 2001. The influence of confining walls on the pressure drop in packed beds. Chem. Eng. Sci. 56 (14), 4321–4329. https://doi.org/10.1016/S0009-2509(00)00533-9

Ertl, G., Knözinger, H., Weitkamp, J., et al., 1997. Handbook of Heterogeneous Catalysis. Vol. 2. VCH Weinheim. https://doi.org/10.1002/9783527610044

Felthouse, T.R., Burnett, J.C., Horrell, B., Mummey, M.J., Kuo, Y.-J., 2001. Maleic Anhydride, Maleic Acid, and Fumaric Acid. John Wiley & Sons, Ltd. Vol. 15. pp. 1–49. https://doi.org/10.1002/0471238961.1301120506051220.a01.pub2

Gascón, J., Valenciano, R., Téllez, C., Herguido, J., Menéndez, M., 2006. A generalized kinetic model for the partial oxidation of *n*-butane to maleic anhydride under aerobic and anaerobic conditions. Chem. Eng. Sci. 61 (19), 6385–6394. https://doi.org/10.1016/j.ces.2006.05.023

Guan, M., Kishi, A., Linak, E., Buchholz, U., 2018. Maleic anhydride. In: Chemical Economics Handbook. IHS Markit.

Hofmann, S., Turek, T., 2017. Process intensification of *n*-butane oxidation to maleic anhydride in a millistructured reactor. Chem. Eng. Technol. 40 (11), 2008–2015. https://doi.org/10.1002/ceat.201700093

Ihli, J., Bloch, L., Böcklein, S., Rzepka, P., Burghammer, M., Cesar da Silva, J., Mestl, G., Anton van Bokhoven, J., 2021. Evolution of heterogeneity in industrial selective oxidation catalyst pellets. ACS Catal. 11 (13), 8274–8283. https://doi.org/10.1021/acscatal.1c01744

Kutscherauer, M., Anderson, S.D., Böcklein, S., Mestl, G., Turek, T., Wehinger, G.D., 2024. A conjugated heat and mass transfer model to implement reaction in particle-resolved CFD simulations of catalytic fixed bed reactors. Eng. Appl. Comput. Fluid Mech. 18 (1), 2292100. https://doi.org/10.1080/19942060.2023.2292100

Lerou, J.J., Mills, P.L., 1993. Du pont butane oxidation process. In: Precision Process Technology: Perspectives for Pollution Prevention. Springer, pp. 175–195. https://doi.org/10.1007/978-94-011-1759-3_13

Lesser, D., Mestl, G., Turek, T., 2016. Transient behavior of vanadyl pyrophosphate catalysts during the partial oxidation of *n*-butane in industrial-sized, fixed bed reactors. Appl. Catal. A Gen. 510, 1–10. https://doi.org/10.1016/j.apcata.2015.11.002

Lesser, D., Mestl, G., Turek, T., 2017. Modeling the dynamic behavior of industrial fixed bed reactors for the manufacture of maleic anhydride. Chem. Eng. Sci. 172, 559–570. https://doi.org/10.1016/j.ces.2017.06.049

Lohbeck, K., Haferkorn, H., Fuhrmann, W., Fedtke, N., 2000. Maleic and Fumaric Acids. John Wiley & Sons, Ltd. Vol. 22. pp. 145–155. https://doi.org/10.1002/14356007.a16_053

Lorences, M.J., Patience, G.S., Diez, F.V., Coca, J., 2003. Butane oxidation to maleic anhydride: kinetic modeling and byproducts. Ind. Eng. Chem. Res. 42 (26), 6730–6742. https://doi.org/10.1021/ie0302948

Müller, M., Junge, K., Mestl, G., Turek, T., 2020a. Millistructured reactor as tool for investigating the kinetics of maleic anhydride synthesis. Chem. Ing. Tech. 92 (5), 575–581. https://doi.org/10.1002/cite.201900131

Müller, M., Kutscherauer, M., Böcklein, S., Mestl, G., Turek, T., 2020b. On the importance of by-products in the kinetics of *n*-butane oxidation to maleic anhydride. Chem. Eng. J. 401, 126016. https://doi.org/10.1016/j.cej.2020.126016

Müller, M., Kutscherauer, M., Böcklein, S., Mestl, G., Turek, T., 2021. Improved kinetics of *n*-butane oxidation to maleic anhydride: the role of byproducts. Ind. Eng. Chem. Res. 60 (1), 218–229. https://doi.org/10.1021/acs.iecr.0c05029

Müller, M., Kutscherauer, M., Böcklein, S., Wehinger, G.D., Turek, T., Mestl, G., 2022. Modeling the selective oxidation of *n*-butane to maleic anhydride: from active site to industrial reactor. Catal. Today 387, 82–106. https://doi.org/10.1016/j.cattod.2021.04.009

Raquez, J.-M., Nabar, Y., Narayan, R., Dubois, P., 2008a. In situ compatibilization of maleated thermoplastic starch/polyester melt-blends by reactive extrusion. Polym. Eng. Sci. 48 (9), 1747–1754. https://doi.org/10.1002/pen.21136

Raquez, J.-M., Nabar, Y., Srinivasan, M., Shin, B.-Y., Narayan, R., Dubois, P., 2008b. Maleated thermoplastic starch by reactive extrusion. Carbohydr. Polym. 74 (2), 159–169. https://doi.org/10.1016/j.carbpol.2008.01.027

Schulz, C., Pohl, F., Driess, M., Glaum, R., Rosowski, F., Frank, B., 2018. Selective oxidation of *n*-butane over vanadium phosphate based catalysts: reaction network and kinetic analysis. Ind. Eng. Chem. Res. 58 (7), 2492–2502. https://doi.org/10.1021/acs.iecr.8b04328

Siemens Industry Software Limited, 2024. gPROMS process release 2023.2.1. https://www.siemens.com/global/en/products/automation/industry-software/gproms-digital-process-design-and-operations.{html}.

Taheri, H., 1992. Continuous Process for the Production of Maleic Anhydride from a C$_4$-Hydrocarbon Feedstock. US Patent 5117007 A.

Trifirò, F., Grasselli, R.K., 2014. How the yield of maleic anhydride in *n*-butane oxidation, using VPO catalysts, was improved over the years. Top. Catal. 57, 1188–1195. https://doi.org/10.1007/s11244-014-0285-5

Uihlein, K., 1993. Butanoxidation an VPO-Wirbelschichtkatalysatoren. Ph.D. thesis. Universität Karlsruhe.

Volta, J.-C., 2000. Vanadium phosphorus oxides, a reference catalyst for mild oxidation of light alkanes: a review. C. R. Acad. Sci. 3 (9), 717–723. https://doi.org/10.1016/S1387-1609(00)01168-3

Wellauer, T., Cresswell, D.L., Newson, E.J., 1981. Heat transfer in packed reactor tubes suitable for selective oxidation 196, 527–542. https://doi.org/10.1021/bk-1982-0196.ch041

Wellauer, T.P., Cresswell, D.L., Newson, E.J., 1986. Optimal policies in maleic anhydride production through detailed reactor modelling. Chem. Eng. Sci. 41 (4), 765–772. https://doi.org/10.1016/0009-2509(86)87156-1

Wilkinson, S.K., Simmons, M., Stitt, E.H., Baucherel, X., Watson, M.J., 2013. A novel approach to understanding and modelling performance evolution of catalysts during their initial operation under reaction conditions–case study of vanadium phosphorus oxides for *n*-butane selective oxidation. J. Catal. 299, 249–260. https://doi.org/10.1016/j.jcat.2012.11.027

Zehner, P., Schlünder, E.U., 1972. Einfluß der Wärmestrahlung und des Druckes auf den Wärmetransport in nicht durchströmten Schüttungen. Chem. Ing. Tech. 44 (23), 1303–1308. https://doi.org/10.1002/cite.330442305